Joint Analysis of Convective Structure from the APR-2 Precipitation Radar and the DAWN Doppler Wind Lidar During the 2017 Convective Processes Experiment (CPEX)

5 F. Joseph Turk[1], Svetla Hristova-Veleva[1], Stephen L. Durden[1], Simone Tanelli[1], Ousmane Sy[1], G. David Emmitt[2], Steve Greco[2], Sara Q. Zhang[3]

[1]Jet Propulsion Laboratory, California Institute of Technology, Pasadena CA 91107 USA
[2]Simpson Weather Associates, Charlottesville VA 22902 USA
[2]Global Modeling and Assimilation Office (GMAO), Goddard Space Flight Center, Greenbelt MD 20771 USA

10 *Correspondence to*: F. Joseph (Joe) Turk (jturk@jpl.caltech.edu)

Abstract. The mechanisms linking convection and cloud dynamical processes is a major factor in much of the uncertainty in both weather and climate prediction. Further constraining the uncertainty in convective cloud processes linking 3-D air motion and cloud structure through models and observations is vital for improvements in weather forecasting, and understanding limits on atmospheric predictability.   To date, there have been relatively few airborne observations
15 specifically targeted for linking the 3-D air motion surrounding developing clouds to the subsequent development (or non-development) of convective precipitation. During the May-June 2017 Convective Processes Experiment (CPEX), NASA DC-8-based airborne observations were collected from the JPL Ku/Ka-band Airborne Precipitation Radar (APR-2) and the 2-um Doppler Aerosol Wind (DAWN) lidar during approximately 100 flight hours. For CPEX, the APR-2 provided vertical air motion and structure of the cloud systems in nearby precipitating regions where DAWN is unable to sense. Conversely,
20 DAWN sampled vertical wind profiles in aerosol-rich regions surrounding the convection, but is unable to sense the wind field structure within most clouds. In this manuscript, the complementary nature of these data are presented from the June 10-11 flight dates, including the APR-2 precipitation structure and Doppler wind fields, and adjacent wind profiles from the DAWN data.

1   Introduction.

25 The mechanisms linking convection and cloud dynamical processes is a major factor in much of the uncertainty in both weather and climate prediction. The associated mesoscale convective systems (MCS) produce much of the Earth's rainfall and are responsible for the bulk of the heat and moisture transport from the Earth's surface into the upper troposphere. The cold pool dynamics are thought to be an important mechanism to facilitate the development of MCSs in the tropical atmosphere (*Chen et. al.*, 2015; *Zuidema et. al.*, 2017), as well as interactions between individual isolated convective storms
30 (*Raymond et. al.,* 2015). These atmospheric boundaries can have significant impact on deep convection, affecting its

initiation, updraft strength and longevity. The intensity and size of the cold pools is strongly dependent upon the vertical distribution of the temperature and humidity and the vertical shear of the horizontal wind. While the overall processes responsible for these interactions have been identified for some time, their precise nature and interactions remains under-constrained by observations, due to the difficulty in obtaining accurate, vertically resolved pressure, temperature, wind and water vapor in the proximity of developing convective clouds. Moreover, increasing evidence points to control of convection by the relatively smaller and more variable amount of moisture above the boundary layer, in the free troposphere (*Schiro and Neelin*, 2019). Further constraining the uncertainty in convective cloud processes *linking 3-D air motion and cloud structure* through models and observations is vital for improvements in weather forecasting and understanding limits on atmospheric predictability.

The resolution of the precipitation radar onboard the Tropical Rainfall Measuring Mission (TRMM; 1997-2014) and the subsequent Global Precipitation Measurement (GPM; 2014-current) missions (4-km horizontal resolution; 250-m vertical) have enabled numerous observational-based studies of MCS convective structure and features (*Jiang et. al.*, 2011). However, the dynamical (air motion) wind field associated with MCS features at this scale not well-represented by current space-based wind profile observing capabilities. The majority of available atmospheric wind observations are primarily water vapor and cloud-tracked atmospheric motion wind vectors (AMV) derived from operational geostationary satellites (*Velden et. al*, 2005), which can be refreshed as quickly as 15-minutes, but are mainly indicative of large-scale mid-to-upper level air motion patterns. Observations of wind vectors in the periphery of smaller-scale cloud systems, especially in the 2-km nearest the Earth (the approximate delineation of the boundary layer) are much less abundant. Outside of ground-based profiling networks, very few over-ocean wind profile observations at a similar GPM-like horizontal resolution are available.

A space-based Doppler wind lidar (DWL) capability has been envisioned as one means to overcome this observational shortcoming (*Baker et. al.*, 2014). Over the past decade, airborne DWL field campaigns have been conducted (*Lux et. al.*, 2018), recently in preparation for the deployment (August 2018) of the first-ever spaceborne DWL, the Atmospheric Dynamics Mission (ADM-Aeolus) of the European Space Agency (ESA) (*Stoffelen et. al.*, 2005). Aeolus provides vertical profiles of the horizontal line-of-sight (LOS) winds at an ≈100-km horizontal resolution and 200-km separation between profiles, with a main application to numerical weather prediction data assimilation (*Horányi et. al.*, 2015). Observations from campaigns with a DWL such as the THORPEX Pacific Asian Regional Campaign (TPARC) were largely focused towards improvement of tropical cyclone forecasts (*Pu et. al.*, 2010). These airborne campaigns have validated the capabilities of a DWL to provide wind profiles in the boundary layer (*Bucci et. al.*, 2018; *Zhang et. al.*, 2018). There has been relatively less focus in collection and analysis of airborne DWL observations in relation to the convective processes linking air motion and transport of water vapor near clouds, and the subsequent development (or non-development) of convection. One main reason is that previous campaigns often lacked nadir scanning Doppler precipitation radar capabilities on the same aircraft to enable matched radar-DWL observations. A scanning precipitation radar provides the

65   actual 3-D representation of the condensed water mass field, and the vertical Doppler winds and associated microphysical vertical structure (*Rowe and Houze*, 2014; *Rowe et. al*., 2012). These data provide one means to validate the forecasted model precipitation structure (e.g., presence/absence of convection, timing, location), that results when the DWL wind vectors are assimilated into cloud resolving models.

70   In this manuscript, airborne DWL and Doppler precipitation radar observations are presented from the NASA-sponsored Convective Processes Experiment (CPEX), which took place between 25 May and 24 June 2017, based out of Fort Lauderdale, FL. The goals of CPEX were to improve the understanding of convective processes during initiation, growth, and dissipation, using a combination of observations and cloud-resolving models. In particular, to measure what combinations of environmental structure and observed convective properties such as vertical velocity and reflectivity

75   profiles, result in rapid upscale growth of a convective system into a large organized mesoscale convective system (MCS), or alternatively, result in failure to grow or rapid decay. This manuscript will describe and present only the airborne precipitation radar and DAWN observations; a separate manuscript will present the associated mesoscale model simulations and DAWN data assimilation experiment results (*Zhang et. al.*, 2019).

2   CPEX Overview.

80   During CPEX, sixteen NASA DC-8 airborne missions were flown into the Gulf of Mexico, Caribbean Sea and the Atlantic Ocean. Each date is summarized in Table 1. During each flight, joint observations were collected from the JPL Ku/Ka-band Airborne Precipitation Radar (APR-2)[1] and the 2-um Doppler Aerosol Wind (DAWN) lidar, covering a variety of isolated, scattered, and organized deep convection, totalling approximately 100 flight hours. Intermittent dropsonde data accompanied the DAWN observations for validation purposes, and to provide complementary wind profiles near convection.

85   The dropsondes system used during CPEX was the High Definition Sounding System (HDSS) dropsonde delivery system developed by Yankee Environmental Services (*Black et. al*., 2017). The dropsonde data are not presented in this manuscript.

Flight	Date	Observations
1	27 May 2017	First local science flight; box pattern in central Gulf; clear air only.
2	29 May 2017	Sampling of scattered convection in NW Caribbean; cells at 1813, 1942-2000.
3	31 May 2017	Multiple boxes over Atlantic, near Bahamas and north of Hispaniola; mostly clear but cells at 1936, 2120.
4	1 June 2017	Convective system over eastern Gulf; multiple passes over convection. 25-min data loss at Ka-band due to TWT amplifier breaker trip.

---

[1] In 2015, APR-2 was augmented with an additional W-band (94 GHz) Doppler radar for an expanded APR-3 capability. Owing to logistical details, the W-band radar was unavailable for CPEX in 2017, hence the use of the APR-2 system.

| 5	2 June 2017	Extended E-W box over western and central Gulf; clear areas and some convective cells, for example at 1750, 1928; decaying convection between 1830-1900, 2100-2110.
6	6 June 2017	Convection over eastern Gulf, especially near 1858, 1955-2115, 2105, 2140.
7	10 June 2017	Boxes east of the Bahamas; stratiform with some convection on ascent between 1840-1850, small cells in box 1925, 2004, 2035-2045, 2118, 2140, 2210-2216.
8	11 June 2017	E-W legs over convective system in central Gulf; isolated cells at 1801, 1830, 1850; extensive precipitation on lines starting at 1900, 1920, and N-S line starting 2005.
9	15 June 2017	Caribbean, east of Yucatan; convection near 1920, 1940, 1953, 2010.
10	16 June 2017	Caribbean, boxes east of Yucatan; convection near 1830-1940, 2050-2140.
11	17 June 2017	Caribbean, boxes east of Yucatan; convective cells at 1745, 1800-1815, 2044-2054, 2223; sampled convective system with box pattern between 1900 and 2030.
12	19 June 2017	E-W legs over north-central and northeast Gulf of Mexico, Tropical Storm Cindy; extensive precipitation between 1700-1820, 1840-2005; numerous isolated cells to 2130, then more extensive areas to 2224.
13	20 June 2017	Bow-tie pattern in central Gulf of Mexico; convective system between 1742-1754, cells 1815-1820, very shallow convection 1923, extensive precipitation between 2110-2150.
14	21 June 2017	E-W flight across Gulf of Mexico; isolated cells at 1842, 1942, 2028, 2107, 2124, 2158, 2240; stratiform/transitional between 1925-1937.
15	23 June 2017	Box pattern to east of Bahamas; crossed isolated cells at 1832, 1859, 1910, 1917; multiple lines over area with isolated cells between 1912-1939.
16	24 June 2017	Over and around Cuba; convection at 1744, box pattern cells near 1829, isolated cells 1843-1944; mature cell near 2106, more cells 2112-2143.

90   **Table 1. Summary of CPEX flight dates.**

APR-2 is a 2-frequency Doppler radar, originally developed as an airborne prototype for the second-generation GPM/DPR precipitation radar (*Sadowy et al.*, 2003). The APR-2 has flown in numerous airborne field campaigns outside of CPEX, most recently the ORACLES (2016-2018) and CAMP2Ex (2019) campaigns. APR-2 acquires simultaneous measurements

95   of multiple parameters at both Ku- and Ka-band (14 and 35 GHz, respectively), including co- and cross-polarized radar backscatter, and LOS Doppler velocities of hydrometeors, with a maximum unambiguous velocity of ±27.5 (Ku-band) and ±10.4 (Ka-band) m s^{-1}.   From a nominal 10-km flight altitude, the horizontal resolution at the surface is ~800-m, with a vertical range resolution and sampling of 50- and 30-m (slightly oversampled).   Based upon analysis of radar surface backscatter measurements from CPEX, the reflectivity calibration is accurate to within 1-2 dB.   From these basic

100   measurements, APR-2 can depict the cloud macroscopic structure (extent, vertical air motion) and estimate the microphysical structure (water content, precipitation intensity, hydrometeor size distribution) of the associated precipitation (*Durden et. al.*, 2012).   These resolutions are adequate to capture cloud features down to the resolution typical of high-resolution cloud models, and appropriate for comparison with DAWN wind profiles in the vicinity near isolated, scattered, and organized deep convection.

105 DAWN is NASA's airborne DWL with a 2-micron laser that pulses at 10 Hz (*Kavaya et. al.*, 2014). It has previously participated in the NASA Genesis and Rapid Intensification Processes (GRIP) (2010) and Polar Winds (2014-15) airborne campaigns. DAWN can provide high resolution (4-12 km in the horizontal and 35-150 m in the vertical) wind measurements in clear as well as partly cloudy conditions. The lidar samples the scene in a conical pattern at a constant 30° elevation angle (i.e., 30-degrees off of nadir), and collects LOS wind profiles at up to five azimuth angles located at -45°, -

110 22.5°, 0°, 22.5° and 45° relative to the aircraft flight direction (Figure 1). During CPEX, DAWN also collected LOS data at only two azimuth angles, -45° and 45°. Since these LOS wind profiles view the local wind field from multiple azimuth angles, multiple LOS profiles are analyzed to estimate the vertical profile of the horizontal wind components (u, v) at different pressure levels using the Adaptive Signal Integration Algorithm (ASIA) processing (*Kavaya et. al.*, 2014). DAWN data are available in both the native LOS format, and processed wind vector (u, v) profile format. In this manuscript, the

115 wind vector data are used to evaluate the wind field near clouds captured by the APR-2. The individual LOS data are projected (along the viewing direction) through the APR-2 radar scan to illustrate the ability of DAWN to sense in and near cloud structures.
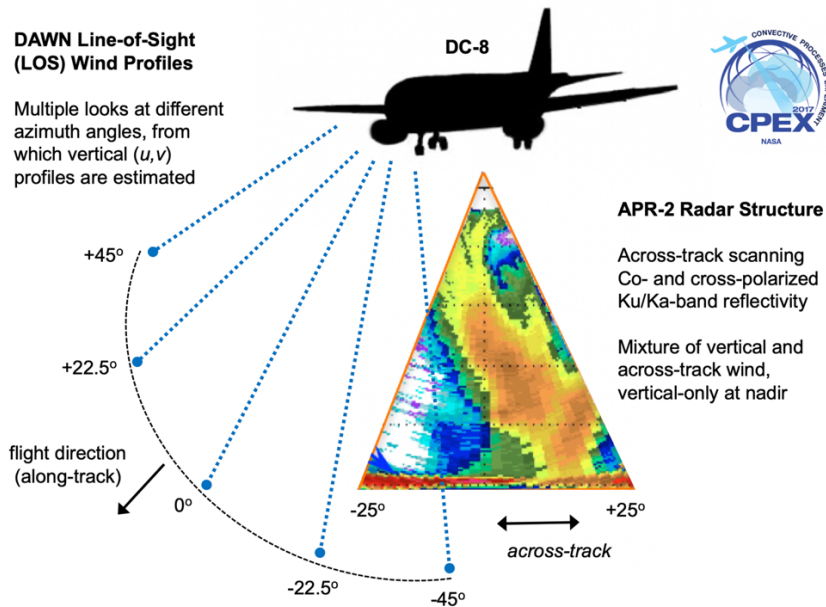
Figure 1: Depiction of DAWN and APR-2 scanning operations from the DC-8 during CPEX. From a 10-km flight altitude, the
120 **APR-2 across track swath width is 8-km, which is approximately the same distance as the separation between the DAWN ground locations of the -45- and +45-degree LOS profile beams.**

5

3 DC-8 Flight Segments on 10 June 2017.

125   The intent of this section is to assess the DAWN sampling density near the cloud systems captured by the APR-2, relative to the cloud evolution. The 10 June 2017 case is highlighted in this section. This case is used since it is a fairly isolated cloud growth case, not greatly affected by large-scale forcing at early stages, and was covered by several repeat DC-8 passes from various directions. On 10 June 2017, the DC-8 took off from Fort Lauderdale near 1800 UTC and headed east towards the area of interest (AOI) with building clouds, located in the box bounded between 24.2N-26.2N latitude and 74W-72W

130   longitude. Figure 2 shows the DC-8 flight tracks on this date, taken from the JPL CPEX Data Portal (**http://cpex.jpl.nasa.gov**) (*Hristova-Veleva et. al.*, 2019), superimposed upon GOES-16 geostationary visible channel imagery from 1902 UTC.
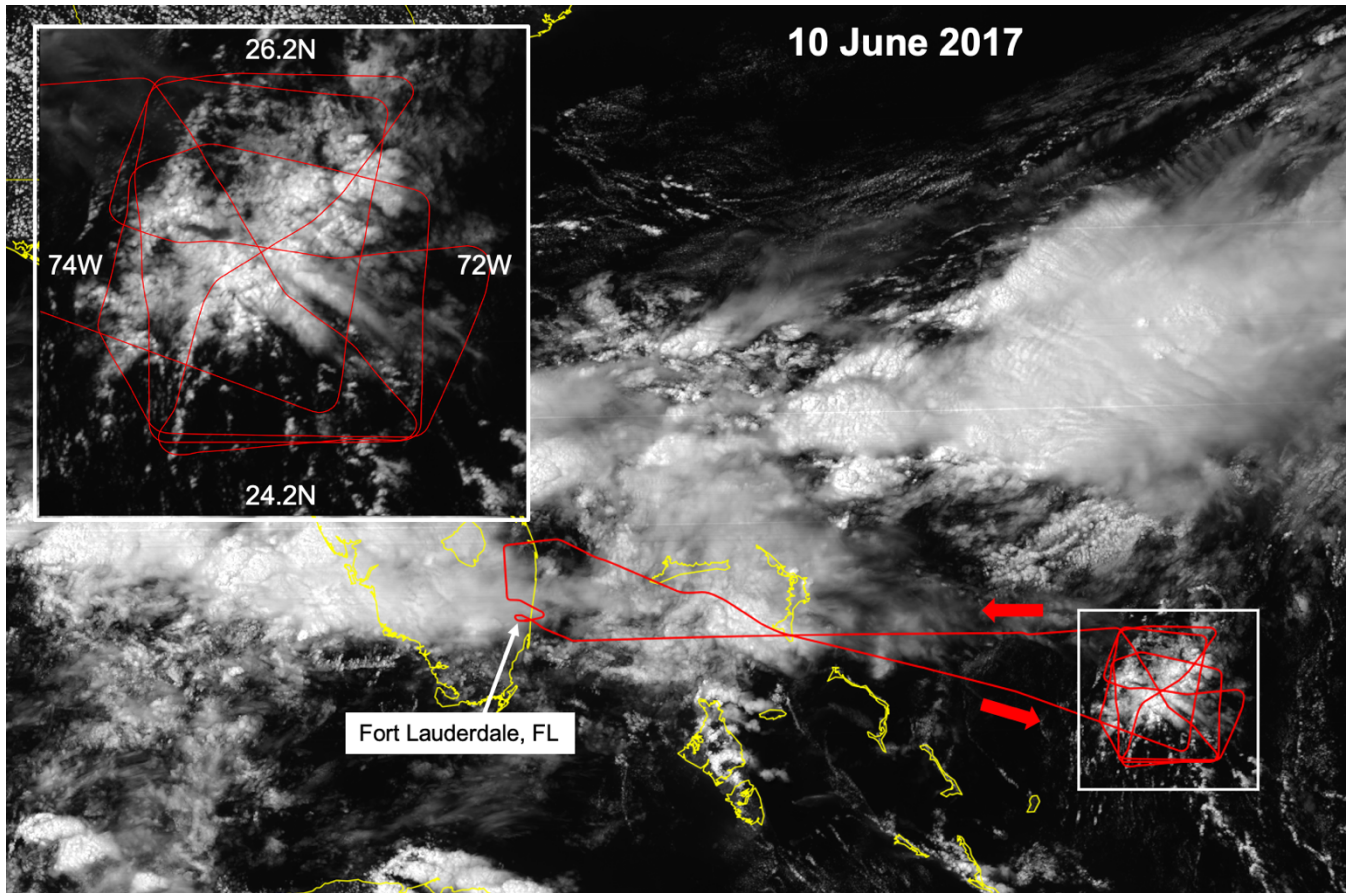
Figure 2: 10 June 2017 flight track (red lines), shown on the JPL CPEX data portal. The DC-8 home base at Fort Lauderdale, FL is indicated. The main area-of-interest is shown in the expanded box, covered by the DC-8 during the 1830-2230 UTC time period. The grayscale background depicts the GOES-16 visible imagery at 1902 UTC.

140 A series of convective box patterns were executed, to sample the evolution of the air movement surrounding the convection from multiple flight bearings. The intent was to be on-station in order to capture developing cumulus clouds before they had developed any significant glaciation, before they reached a stage of vertical development where the DC-8 was unable to overfly from its nominal 10-km flight altitude. A photograph taken from the DC-8 near 2200 UTC (Figure 3) on this date illustrates an example of a cloud at a desired stage of evolution, where the clouds are captured at an early enough stage such

145 that the DC-8 can safely overfly multiple times during subsequent evolution.

Figure 3: View of developing cumulus from the DC-8 window, near 2200 UTC on 10 June 2017, from a 10-km flight altitude.

150

APR-2 data was collected in tandem with DAWN between 1835-2230 UTC. To explain the DAWN observations relative to the development of the precipitation, the analysis is broken into four one-hour segments, separated by the DC-8 flight track segments during each hour. The APR-2 data will be shown in context to give a sense of when and where (proximity and cloud penetration depth) DAWN can provide valid wind data. Furthermore, the analysis will focus on the wind shear within

155 each quadrant (NE=northeast, SE=southeast, SW=southwest, NW=northwest), relative to the approximate center (25.2N 73W) of the AOI flight box in Figure 2.   These segments also correspond to the data assimilation interval used in the investigation of these data by *Zhang et. al*. (2019).

3.1   Flight Segment 1 (1830-1930 UTC).

This first DC-8 flight segment flew along a 120-degree bearing approaching the NW and SW quadrants of the AOI, whereas
160 the next three flight segments discussed below take place inside of the main AOI.   Figure 4 shows the plan view at 2-km (top) and 8-km (bottom) constant elevation levels.   The locations of DAWN wind vectors are shown by the red barbs.   The densest DAWN sampling occurs between 1900-1930 in the mostly cloud-free area, shown in the lower right of Figure 4, with 5-10 m s^{-1} winds at both levels.
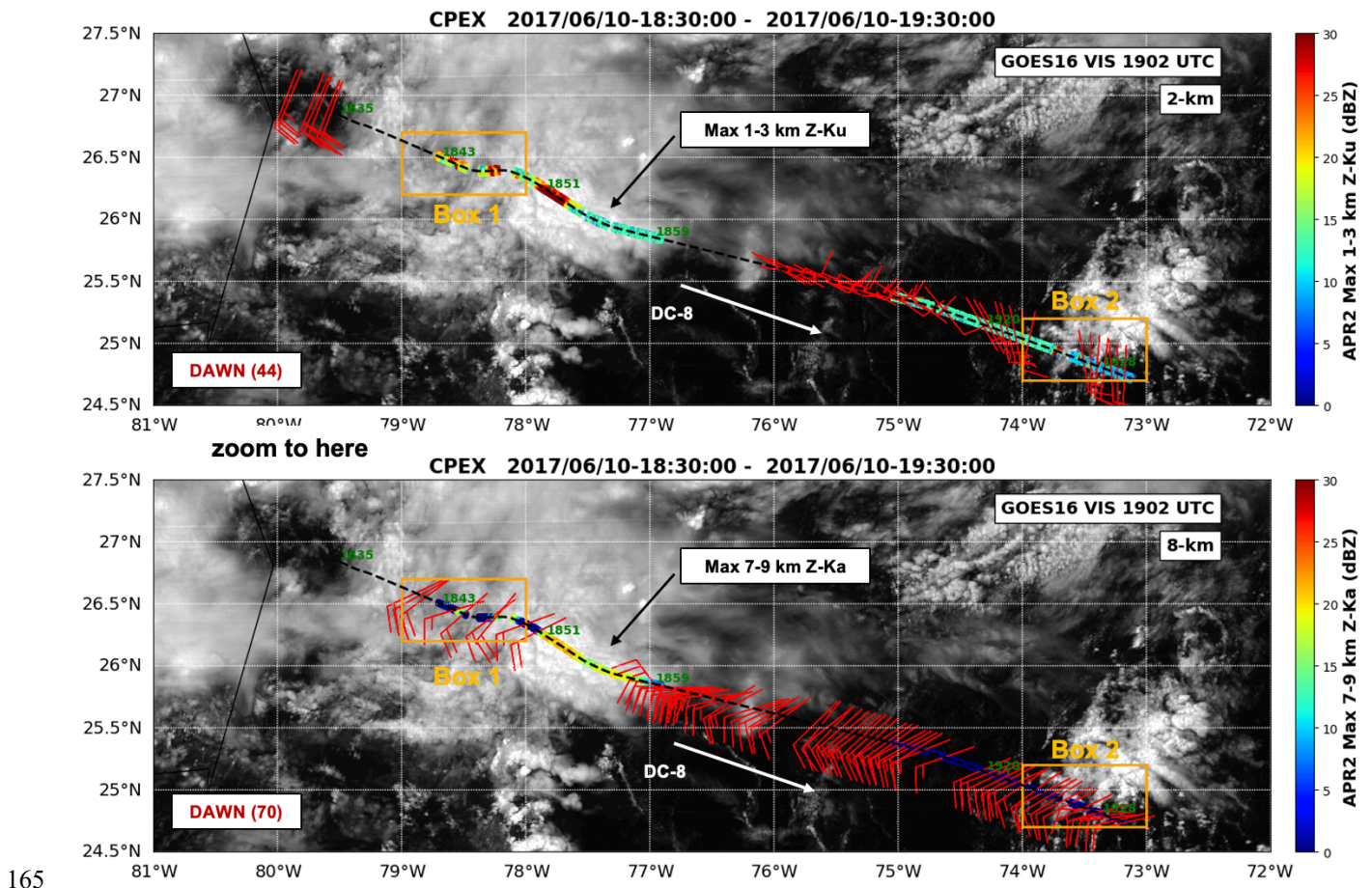
165

Figure 4. DC-8 flight line during segment 1 (1830-1930 UTC) on 10 June 2017. The GOES-16 visible imagery at 1900 UTC is shown in the background grayscale (scaled from 0-100% albedo, not shown). (Top panel): The red barbs show the locations of the wind vectors (44 total) estimated by DAWN at 2-km height.   The background color represents the average APR-2 Ku-band

8

reflectivity between 1-3 km height (top color scale).   (Bottom panel): Same as top panel, but for an 8-km height. The background

170 color represents the APR-2 average Ka-band reflectivity between 7-9 km (bottom color scale).

For the 2-km level, the maximum APR-2 Ku-band reflectivity between 1-3 km is plotted underneath the DAWN winds; for the 8-km level the maximum Ka-band reflectivity between 7-9 km is shown instead (the rationale being that since there is less path attenuation through rain at Ku-band than at Ka-band, the Ku-band data provide a better depiction of the cloud

175 structure for the deeper 2-km level; the APR-2 is more sensitive to clouds at Ka-band than at Ku-band, so the Ka-band reflectivity was used for the higher 8-km level cloud structure). Peak APR-2 Ku-band reflectivity at 2-km exceeded 30 dBZ.

In Figure 4, the associated cloud and aerosol conditions were such that the processing of these DAWN LOS data produced a total of 44 vectors at 2-km height (top), and 70 vectors at 8-km height (bottom). To look in more detail to the DAWN

180 sampling proximity relative to the locations of individual cloud structures sampled by the APR-2, Figure 5 and Figure 6 show zoom-in depictions covering the two boxes indicated with the orange rectangles in Figure 4, which cover a mostly cloudy area (Box 1 from 1835-1855 UTC, Figure 5) and mostly clear area (Box 2 from 1924-1930 UTC, Figure 6), respectively. The mean sea level (MSL) locations of the DAWN LOS profiles are indicated with colored markers. Owing to the conical scan pattern of the five looks shown in Figure 1, the locations appear as a zig-zag pattern as the DC-8 moves

185 forward. Each DAWN LOS beam is colored by the lowest altitude where the SNR > 5 (the 5-dB value is used as a reference level, not as an absolute minimum threshold, as DAWN often provides valid data at lower SNR levels).   The ground locations of the DAWN LOS profiles are indicated with colored markers, and a thin line connected to each marker shows the LOS projection extending from the DC-8 to MSL.

9
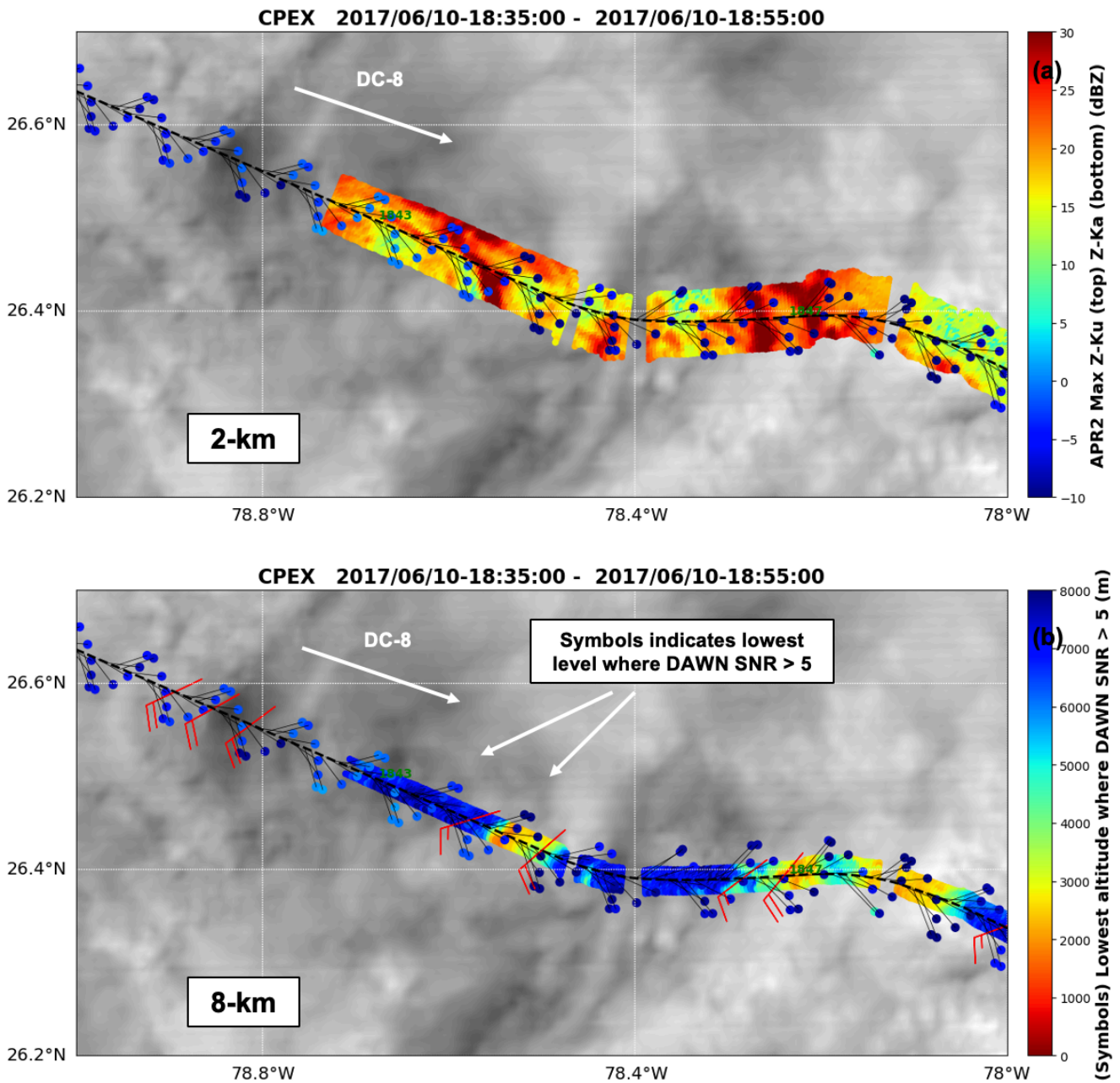
Figure 5. Same as Figure 4, but zoomed in to the flight segment between 1835-1855 UTC (Box 1 in Figure 4). The symbol (dot) colors indicate the lowest level where DAWN SNR > 5 dB (lower panel color scale). Periods of missing APR-2 data indicate no data. (a) 2-km level, (b) 8-km level. DAWN winds at each level are indicated with the red barb symbols.

Note that in the mostly-cloudy Box 1 area (Figure 5), the DAWN sampling pattern is evident, covering about an 8-km swath as the lidar collects samples at each of the five azimuth locations in its conical scan. For these cloud cover conditions, no

10

DAWN wind vectors were estimated at the 2-km height. However, at 8-km height, DAWN processing retrieved wind vectors even where the Ka-band reflectivity in the vicinity was as high as about 15 dBZ, showing about 10 m s^{-1} south-easterly winds. The mostly-clear Box 2 region shown in Figure 6 (1924-1930 UTC) is presented in an identical layout as Figure 5. At this time, DAWN was configured in the 2 looks per scan (-45° and 45° azimuth). In this region, DAWN was able to sense well below 2-km even in the vicinity of clouds at the 10-15 dBZ Ku-band reflectivity level from APR-2, showing 5 m s^{-1} southerly winds at 2-km, becoming more westerly at 8-km height.
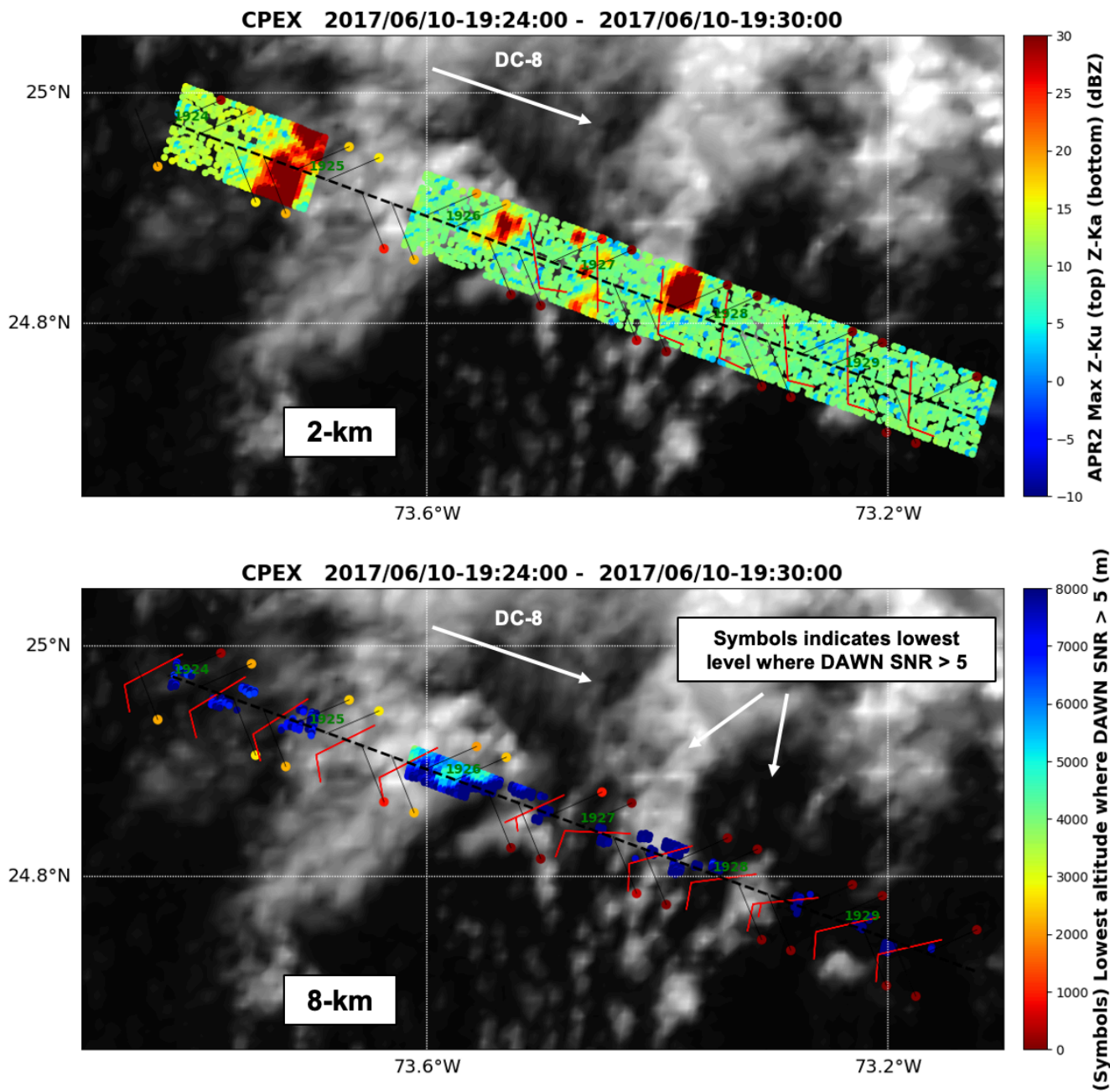
Figure 6. Same as Figure 5, but zoomed in to the flight segment between 1924-1930 UTC (Box 2 in Figure 4).

In these DAWN data, there is a tendency for increased directional shear between these two vertical levels as the DC-8 approaches the AOI. To enhance this feature, the left panel of Figure 7 displays each DAWN profile in Figure 4 in a two-level hodograph form, where each vector points from the DAWN (u,v) wind at 2-km to the (u,v) at 8-km, thereby

representing the shear between these two levels. When the vector is aligned along a radial direction, that indicates no directional shear, only speed shear. When the vector is aligned away from the radial direction, that indicates directional shear and possible speed shear. The shear vectors are colored according to which quadrant (NE, SE, SW, NW) they are located in, relative to the approximate center (25.2N 73W) of the AOI flight box in Figure 2. During this time there is

215 sustained directional wind shear in the SW and NW quadrants, oriented from west to east. A similar analysis for the shear between 2-km and 6-km (right panel of Figure 7) shows the shear oriented more south to north.
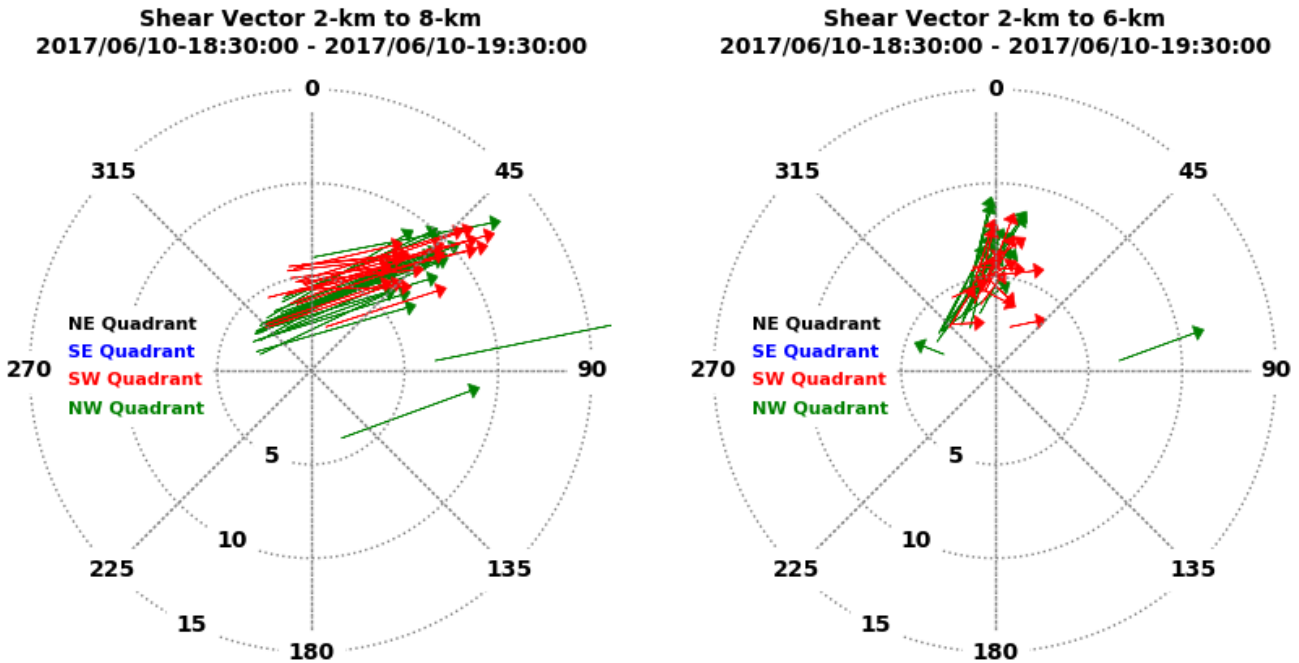
Figure 7. Two-level hodograph derived from the DAWN wind profiles during 1830-1930 UTC in a polar coordinate form. Rings
220 **are spaced at 5 m s⁻¹ intervals. Each vector represents shear derived from each wind profile. (Left) Shear vector pointing from**
(*u,v*) at 2-km towards (*u,v*) at 8-km. (Right) Shear vector pointing from (*u,v*) at 2-km towards (*u,v*) at 6-km. The shear vectors are
colored according to which quadrant (NE=northwest, SE=southeast, SW=southwest, NW=northwest) they are located in, relative
to the approximate center (25.2N 73W) of the AOI flight box in Figure 2. During this time, the DC-8 sampled only the SW and
NW quadrants.
225

To provide a depiction of the DAWN vertical sampling capability, a cross-section of the DAWN vertical profile sampling locations superimposed upon the APR-2 nadir reflectivity is shown in Figure 8. The black points represent locations of valid DAWN (*u, v*) wind vectors during this time. Several notable features are evident. Depending upon the APR-2 transmit

230 pulse length, there is a blind zone (~ 1.8 km) below the aircraft where the radar processor does not receive any returned signals. This is noted in a short period where the cloud tops were within the APR-2 blind zone (near scan 750), but the

cloud top was identifiable in the DAWN profiles (labeled the "upper cloud area" in green shading in Figure 8). Similarly, near the surface where the APR-2 backscatter is affected by ground clutter in the lowest 500-m, DAWN was able to provide wind observations to the surface. In general, DAWN winds are abundant above 6-km (where the SNR is highest), and below

235 3-km (where the aerosol content is higher), with considerable upper level sampling right up to the edges of the tall developed clouds (near scan 1000). There are several DAWN profiles that bump up close to the small convective cell near scan 1800 (denoted with a red ellipse in Figure 8), which are associated with the clouds shown in Figure 6 (Box 2) top panel, where the Ku-band reflectivity exceed 30 dB. To show this area in more detail, Figure 9 zooms in to the Box 2 area (1924-1930 UTC), where three small growing clouds are shown in the middle of this figure. DAWN wind profiles are produced to the surface

240 next to growing convection near scans 100 and 120, but not for the cell near scan 75. This highlights that convective clouds are not continuous "impenetrable" cloud structures, but in nature have gaps or "holes" in them where the DAWN LOS view can penetrate through to lower levels.
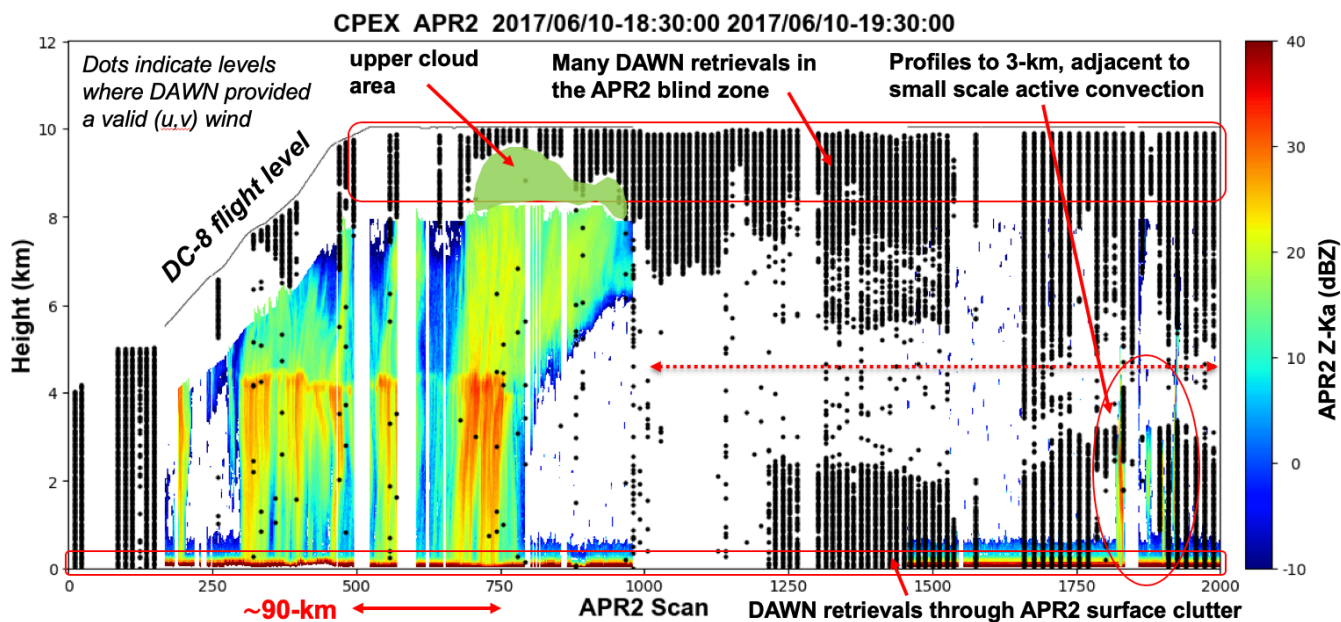
245 **Figure 8. Cross-section of the APR-2 Ka-band reflectivity (color scale in dBZ) during segment 1 (1830-1930 UTC). The x-axis represents the APR-2 scan number (2000 scans representing 720-km ground distance), and y-axis the MSL height (km). The DC-8 reached its nominal 10-km flight altitude near 1840 UTC. The black points represent vertical locations of valid DAWN (u, v) wind vectors produced from the DAWN processing of the LOS data. The green shaded "upper cloud" area shows an area where there are clouds in the 1.8-km blind zone (where APR-2 does not process data), but whose cloud top is noted in the DAWN profiles**

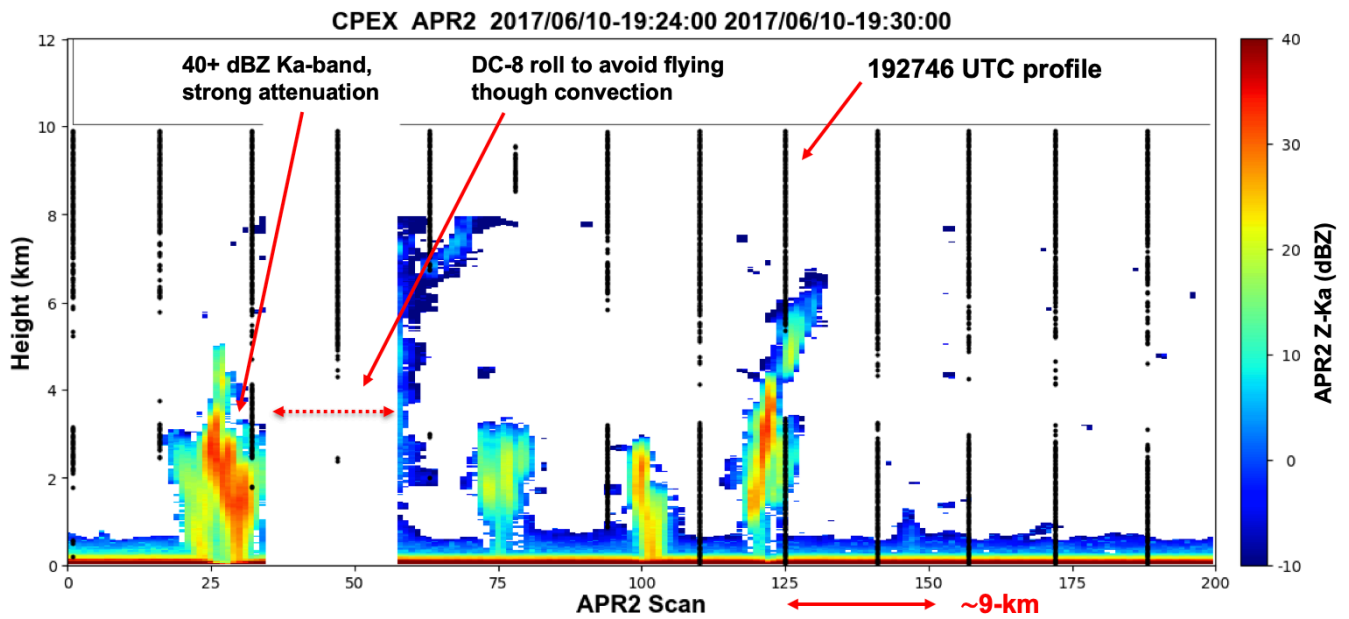250 **above this shaded area.**

14

Figure 9. Same format as Figure 8, but covering only the Box 2 area (1924-1930 UTC) shown in Figure 4.   DAWN wind profiles are obtained to the surface very close to the growing convection near 192746 UTC (near scan 120).

255

3.2   Flight Segment 2 (1930-2030 UTC).

From 1930-2030 UTC, the DC-8 conducted a series of flight legs in a counter-clockwise pattern within the AOI, with densest sampling in the NW and SE quadrants, before departing along a 270-degree bearing. Figure 10 illustrates the APR-2 and DAWN data in the same format as used in Figures 5 and 6. Maximum Ka-band reflectivity in the 7-9 km level are near 20-25 dB in the middle of the segment. On the north side of the AOI, the winds were mainly southwesterly near 10 m s^{-1}, with 2-km level winds more southerly with weaker 5 m s^{-1} speeds.
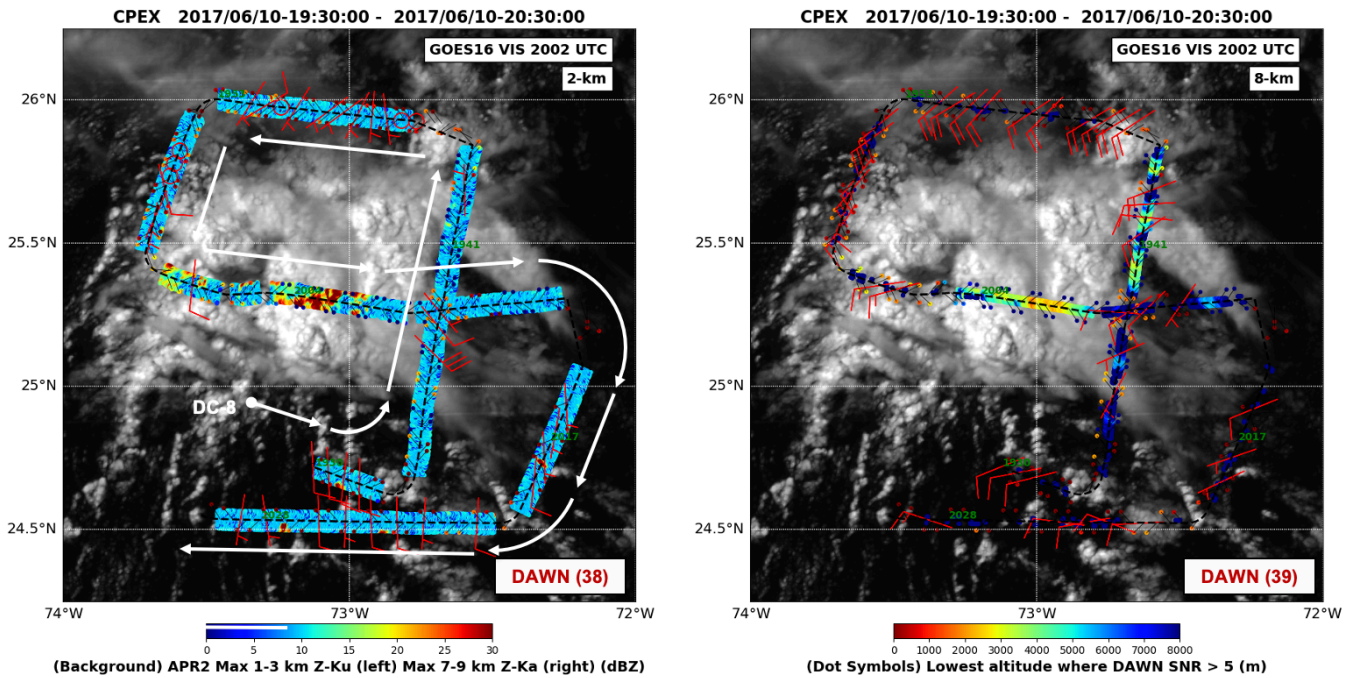
Figure 10. DC-8 flight line during segment 2 (1930-2030 UTC) on 10 June 2017. The GOES-16 visible imagery at 2000 UTC is shown in the background grayscale. DAWN winds at each level are indicated with the red barb symbols. (Left) 2-km level. The background color represents the average APR-2 Ku-band reflectivity between 1-3 km height. (Right): Same as left panel, but for an 8-km height. The background color represents the APR-2 average Ka-band reflectivity between 7-9 km. In both panels, the symbol (dot) colors indicate the lowest level where DAWN SNR > 5 dB (lower panel color scale), according to the color scale on the right panel. Periods of missing APR-2 data indicate no data.

In the NW quadrant of the AOI, there is a large shear magnitude between the 2- and 8-km levels (Figure 11), but it is less directional (vectors more aligned in the radial) compared to Figure 7. In Figure 11, the shear between 2- and 6-km in the NW quadrant (green arrows) is similar to Figure 7, but the shear between 2- and 8-km is pointing more towards the east. The shear between 2- and 8-km in the SW and SE quadrants (red and blue arrows, respectively) points mostly towards the east-southeast directions, but this same signature is not well noted between the 2- and 6-km levels, owing to the reduced DAWN sampling at the 6-km level.

16
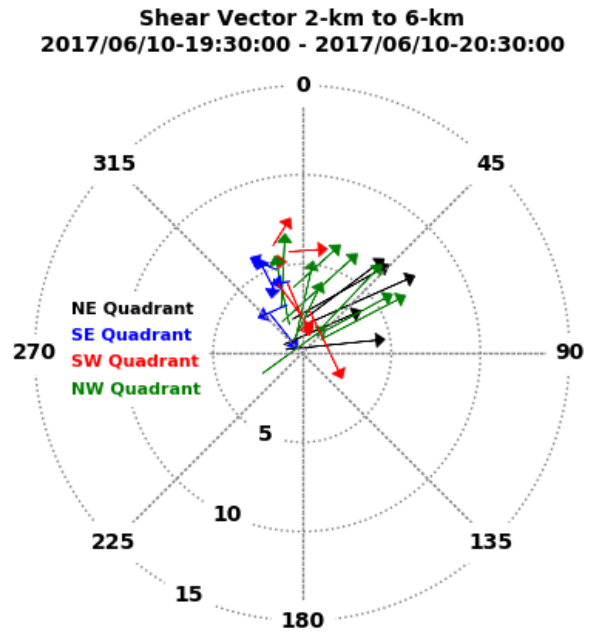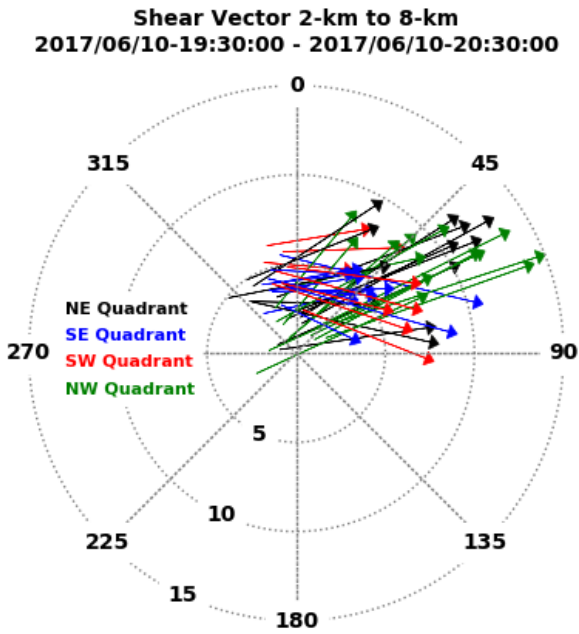
Figure 11. Same as Figure 7, but for flight segment 2 (1930-2030 UTC).

The vertical cross section of the DAWN wind profiles sampling locations alongside the APR-2 nadir reflectivity profile is shown in Figure 12 (areas where the DC-8 was making a banking turn are omitted). Similar to flight segment 1, the two main "no-cloud" regions between APR-2 scans 600-900 and 1300-2000 are well sampled at the upper and lower heights levels. Near scan 850, DAWN data stops near 8-km in areas where APR-2 does not show any cloud, and several profiles near scan 900 sense deeper (to nearly 4-km), both of which may be from lidar backscatter off of clouds not sensed by APR-2 (i.e., below the minimum Ka-band detectability). The lowest-most level retrieved by DAWN near scan 300 and again near scan 1200 appear to be the cloud top, which occurred in the 1.8-km blind zone (~ 8.2-10 km height) area where APR-2 does not provide any data. Near scan 400, there are numerous DAWN profiles provided in cloud gaps as the DC-8 passed through some higher-level clouds.
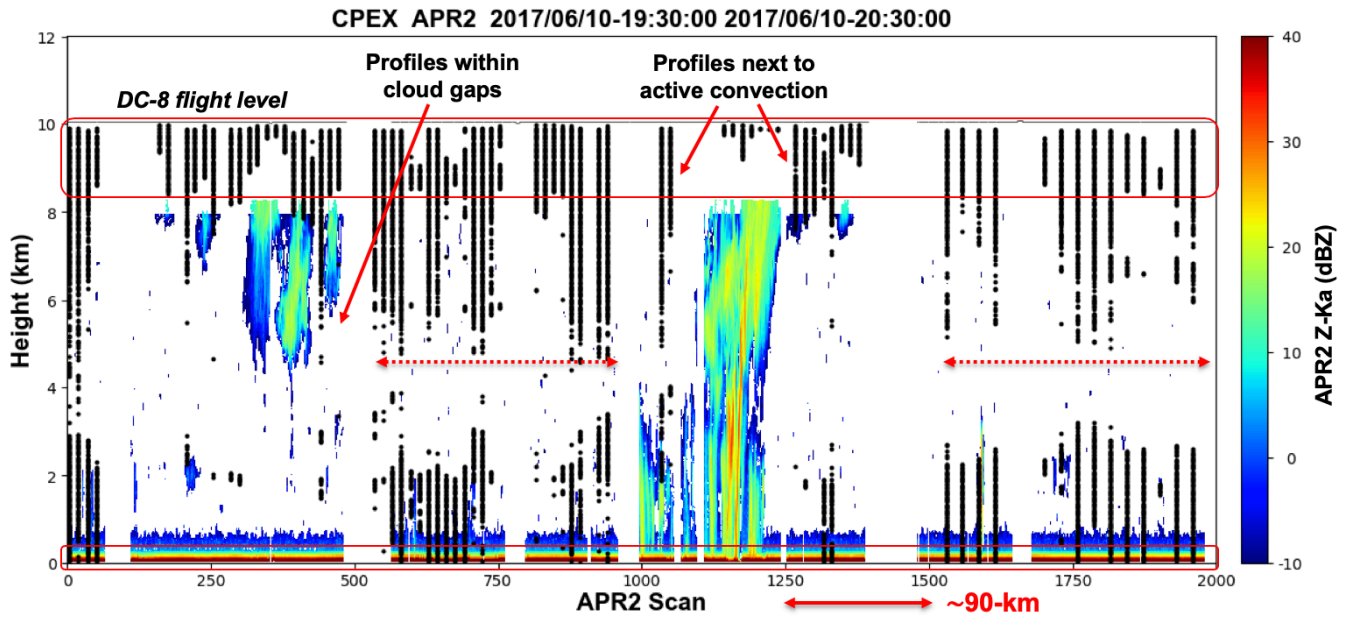
Figure 12. Cross-section of the APR-2 Ka-band reflectivity (color scale to right) during segment 2 (1930-2030 UTC). Same layout and format as Figure 8.

3.3 Flight Segment 3 (2030-2130 UTC).

Flight segment 3 begins with the DC-8 heading in a northerly direction. The flight revisited some of the area sampled during the previous segment by executing a box pattern in clockwise direction, before exiting to the east along a 90-degree bearing (Figure 13). Towards the end of this flight segment, the DC-8 dropped to a 9-km flight level. At 8-km height, 25 DAWN wind vectors were estimated from the LOS data processing.
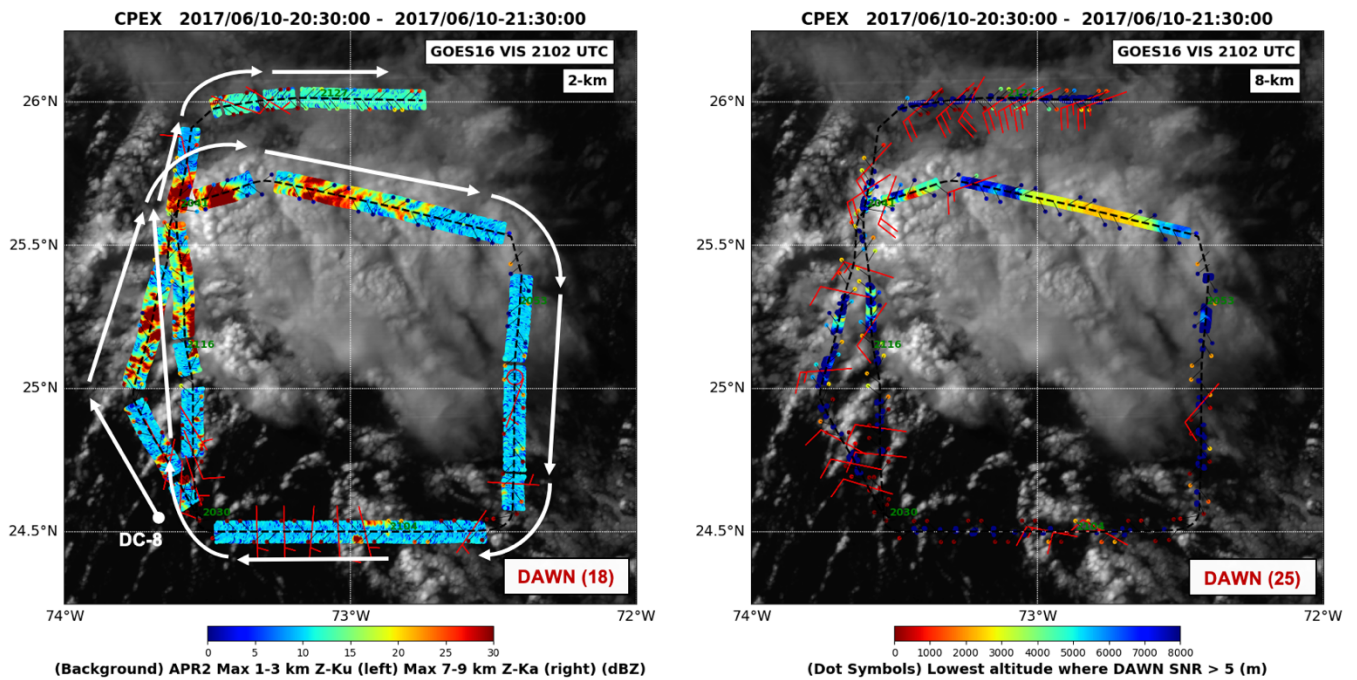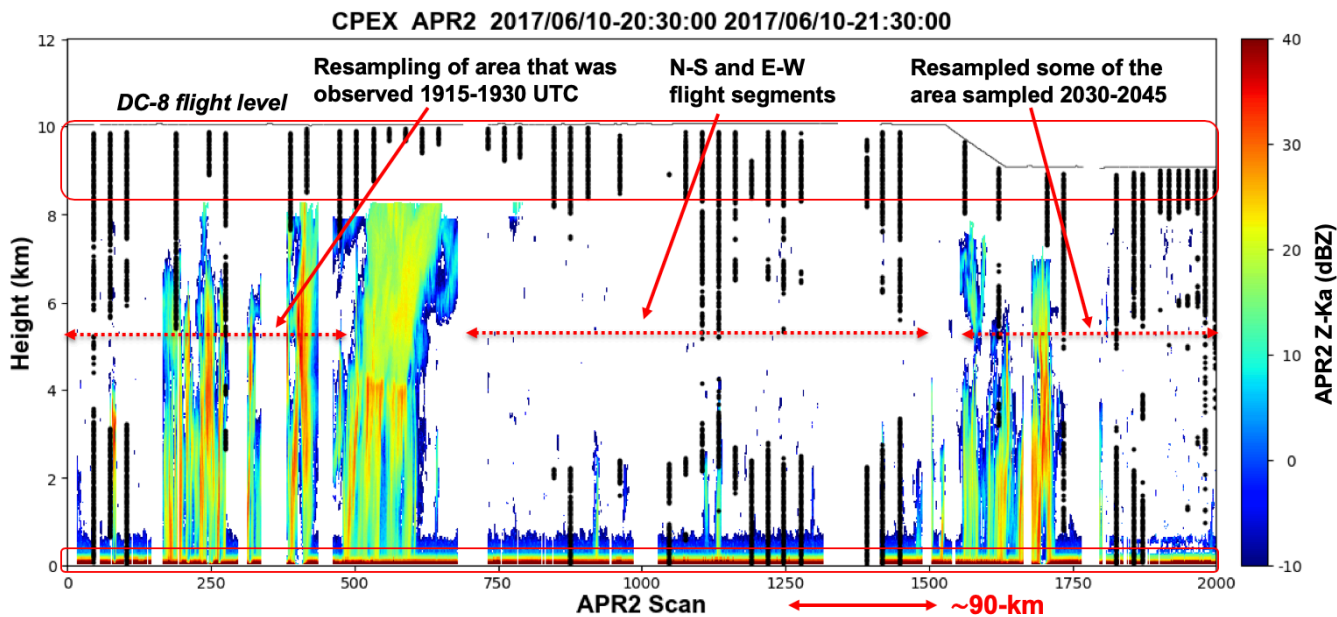
Figure 13. DC-8 flight line during segment 3 (2030-2130 UTC) on 10 June 2017. Same layout and format as Figure 10.

305 The 90-degree directional shear on the SW quadrant of the AOI is still present, measuring about 5 m s^{-1} in magnitude (Figure 14), but insufficient 8-km winds were obtained in the other quadrants for comparison (at the 2-km level, only 18 DAWN wind vectors were estimated, nearly all concentrated on the south side of the AOI).
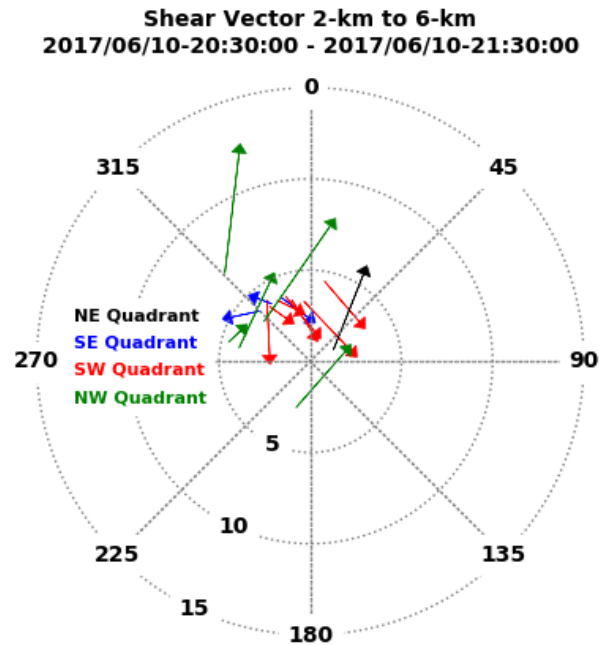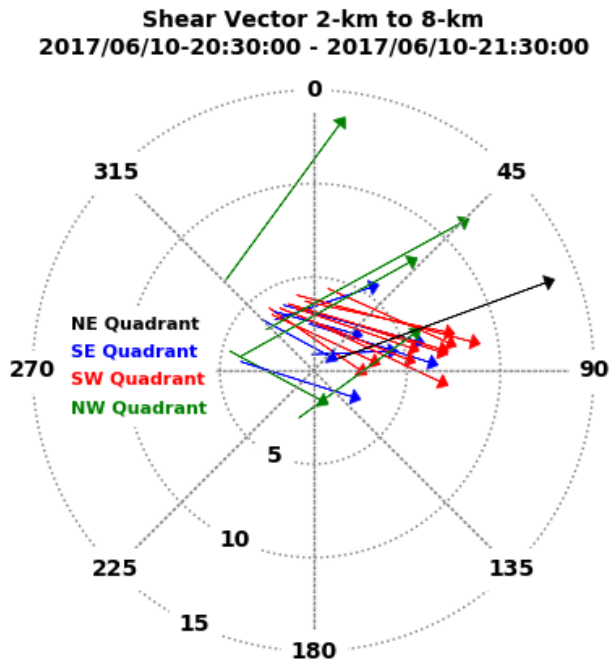
Figure 14. Same as Figure 5, but for flight segment 3 (2030-2130 UTC).

Figure 15 shows the DAWN vertical sampling density during this flight segment relative to the APR-2 Ka-band reflectivity structure. On the east side of the AOI the DC-8 passed above a region of thin clouds (as shown in the IR background in Figure 11), but were below the sensitivity of APR-2. This could be one reason for the reduced DAWN sampling between APR-2 scans 700-1000 in the 2-8 km height level, but the E-W leg (scans 1200-1400) provided DAWN profiling to the surface in many locations.

Figure 15. Cross-section of the APR-2 Ka-band reflectivity (color scale to right) during segment 3 (2030-2130 UTC). Same layout and format as Figure 8.

3.4 Flight Segment 4 (2130-2230 UTC).

Flight segment 4 begins with the DC-8 heading in an easterly direction and then banking to a 225-degree bearing. The DC-8 partially completed a figure-eight pattern, before exiting to the west along a 270-degree bearing and returning to Florida, as shown in Figure 16. The total DAWN profile sampling numbers are higher than segment 3, with 49 and 63 DAWN vectors provided at 2- and 8-km heights, respectively. The cloud system near 25.5N 73.5W has matured considerably relative to its structure in previous flight segments, represented with a fairly well-defined melting level shown near scans 1450-1550.
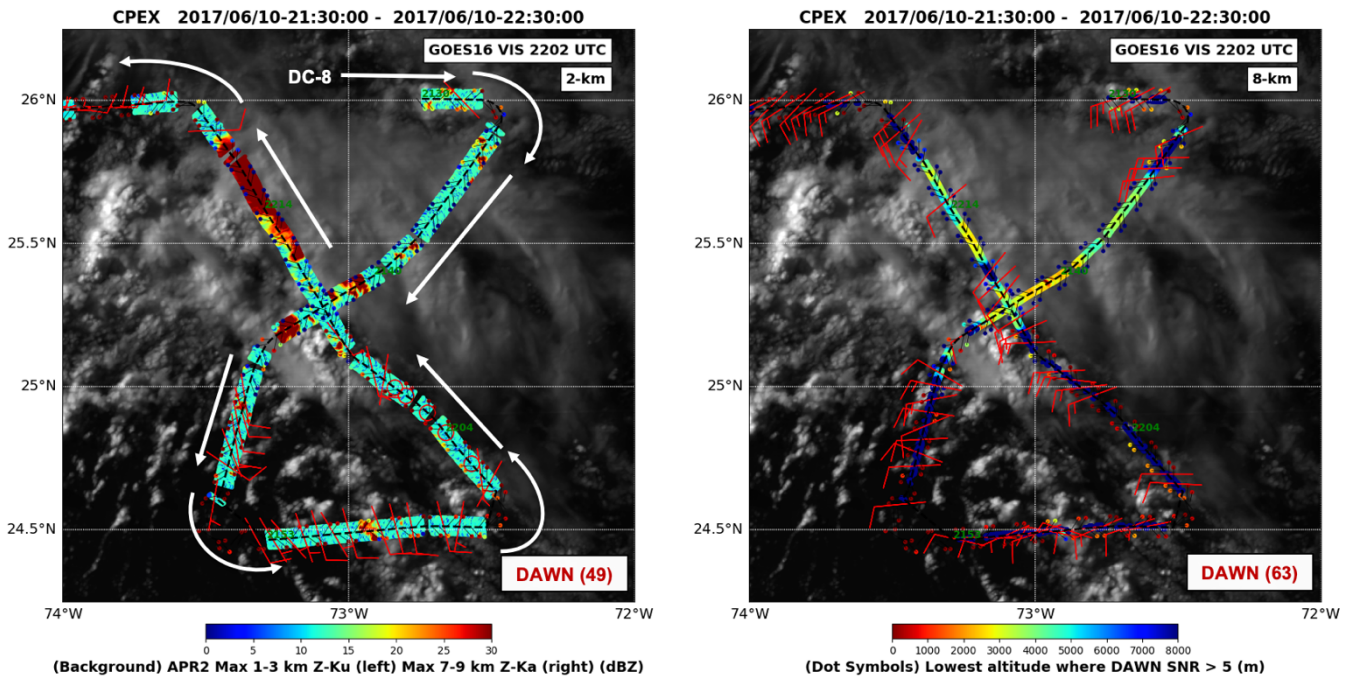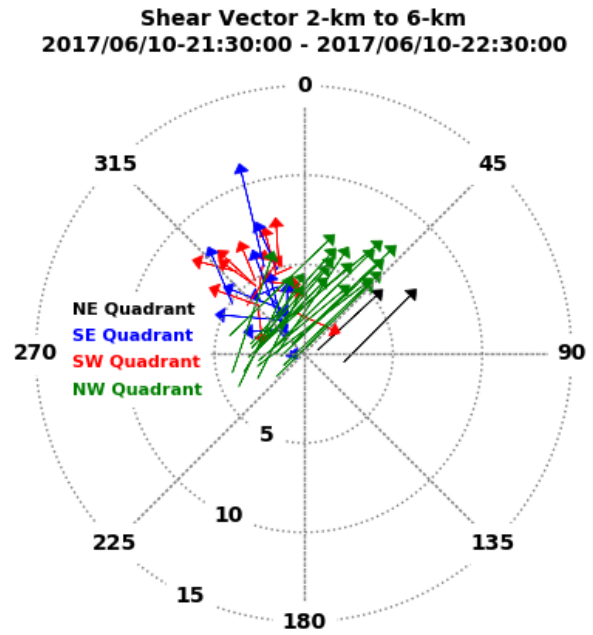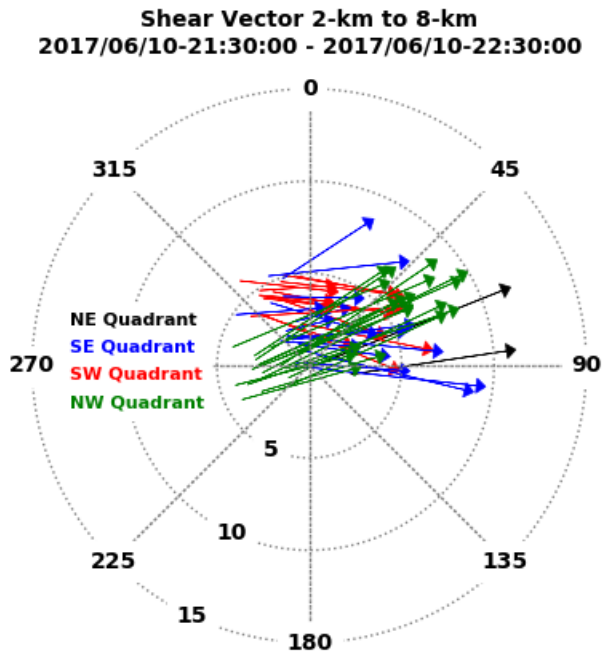
Figure 16. DC-8 flight line during segment 4 (2130-2230 UTC) on 10 June 2017. Same layout and format as Figure 10.

335   Figure 17 shows the shear in the NW quadrant between 2- and 8-km (and between 2-km and 6-km), pointing towards the northeast along a near-radial direction (little directional shear). This period also gathers sufficient DAWN data in the SE quadrant (blue vectors) that was not well sampled in the earlier time segments. This shows evidence of shear between 2-km and 6-km pointing to the north, but shear between 2-km and 8-km pointing towards the east.

Shear Vector 2-km to 8-km
2017/06/10-21:30:00 - 2017/06/10-22:30:00

Shear Vector 2-km to 6-km
2017/06/10-21:30:00 - 2017/06/10-22:30:00

NE Quadrant
SE Quadrant
SW Quadrant
NW Quadrant

Figure 17. Same as Figure 5, but for flight segment 4 (2130-2230 UTC).

Narrow growing clouds were first overflown during scans 200-400 (Figure 18). DAWN vertical sampling density during this time is fairly dense, with more winds provided in the 2-6 km height level than during flight segment 3, notably in the middle and end of this flight segment. When the DC-8 moved to a lower 9-km flight level, the pulse width was changed resulting in the APR-2 blind zone being shorted by one-half (to 0.9 km), which is evident for the tallest clouds near scans 400 and 1400. DAWN also provided overall better sampling in the mid-levels from this lower flight altitude, with almost complete top-bottom profiles towards the end of the flight segment.

23
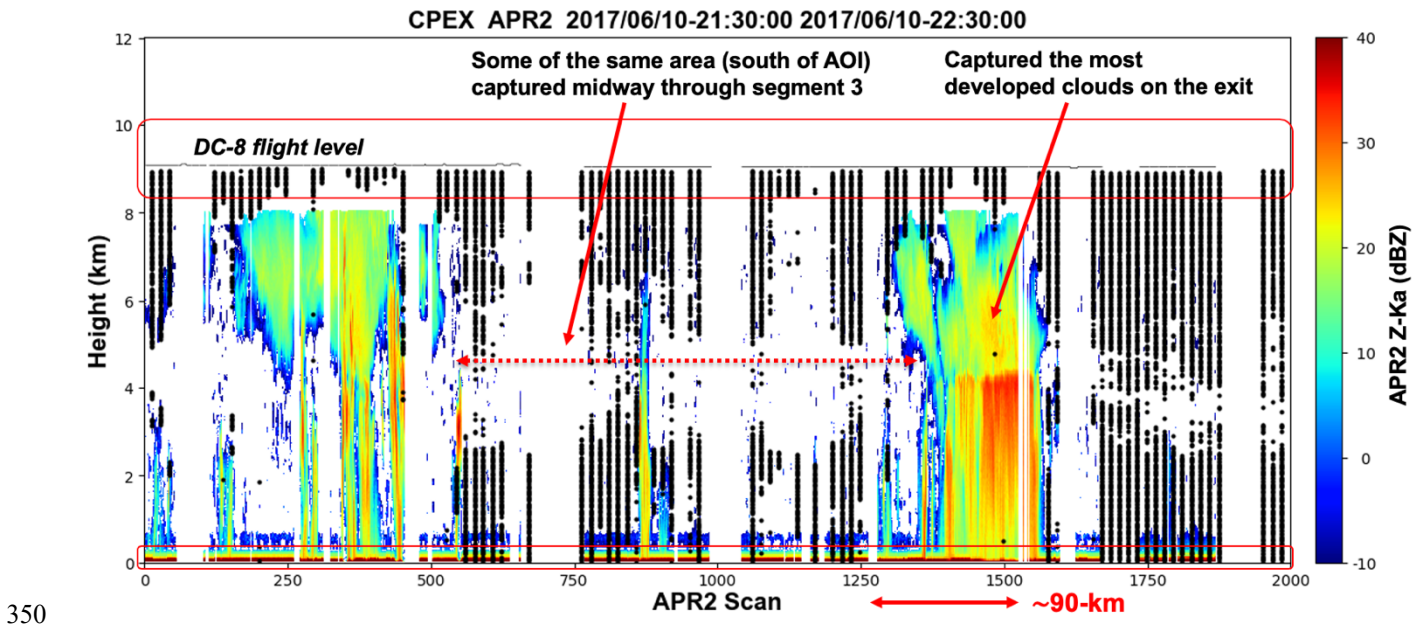
Figure 18. Cross-section of the APR-2 Ka-band reflectivity (color scale to right) during segment 4 (2130-2230 UTC). Same layout and format as Figure 8.

4   DAWN and APR-2 horizontal winds on 11 June 2017.

APR-2 also provided vertical air motion and structure of the cloud systems in the cloud-detected regions where the DAWN profiling capability was degraded. The purpose of this section is to examine a method to couple the two wind estimates near clouds. By viewing clouds from multiple viewing directions near nadir, airborne Doppler radars sample a mixture of the vertical and horizontal winds associated with the movement of the hydrometeors being sensed (*Heymsfield et. al.*, 1996). As the DC-8 moves forward and the APR-2 scans across-track, the measured Doppler velocity represents a combination of the vertical and across-track components of the hydrometeor motion within each APR-2 range bin (*Durden et. al.*, 2003). These data can provide some complementary wind direction information to complement DAWN, and under the right conditions (no significant horizontal shear across the APR-2 scan swath) provide some continuity in the wind measurements between the cloud and no-cloud areas. The received Doppler velocity represents contributions from the motion of the hydrometeors owing to air motion, and the contribution owing to the (reflectivity-weighted) hydrometeor fall speed. Define θ as the viewing angle from nadir (e.g., zero represents straight downward, and negative and positive denote the left and right sides of the APR-2 swath, respectively), and v_z and v_y as the vertical and across-track wind components. Then the Doppler wind at corresponding left and right sides of the swath is given by:

$$v_{left} = v_z cos|\theta| - v_y sin|\theta| \tag{1}$$

24

370 $v_{right} = v_z cos|\theta| + v_y sin|\theta|$ (2)

where the subscripts left and right refer to the corresponding APR-2 beam positions at $-\theta$ (left side of swath) and $+\theta$ (right side of swath), respectively. The vertical (z) and across-track (y) wind components are easily solved for,

375 $v_z = (v_{right} + v_{left})/2cos|\theta|$ (3)

$v_y = (v_{right} - v_{left})/2sin|\theta|$ (4)

Note that in this formulation, the effects owing to the hydrometeor fall speeds are still included, so the estimate of v_z in (3) is
380 not the same as the vertical (*w* component) wind due to air motion only.   To account for the fall speed, the fall speed-reflectively relation developed by Black et al. (1996) is applied and only the 8-km level winds (where there has not yet been significant attenuation) are assessed.   After this correction, v_z is assumed equal to the *w* wind owing to air motion. However, in general more rigorous radar inversion methods that account for the radar attenuation and the hydrometeor Doppler fall speed are required before this formulation can be applied to lower cloud levels (*Guimond et. al.*, 2014)

385

This principle is examined on the APR-2 data gathered between 1800-2100 on 11 June 2017. Figure 19 shows the plan view, where there are abundant DAWN wind vectors at 8-km, including many that are close to clouds. There are six flight legs along a predominant 90-degree (W-E) or 270-degree (E-W) (+*u* and -*u* wind component direction, respectively) flight bearings, beginning near 1800, 1815, 1838, 1900, 1920 and 1955 UTC (with some slight deviations along these directions to
390 avoid deep clouds near flight level). The first and last three of these flight legs occurred in predominantly cloud-free and cloud-covered conditions, respectively. The top panel of Figure 20 shows the time intervals corresponding to these 90- and 270-degree bearings. In these flight directions, the APR-2 across-track wind component v_y (4) is solely contributed by the *v* wind. When the DC-8 transitions from a 90- to 270-degree flight bearing (or vice-versa), a flip in the sign of the APR-2 v_y component is expected, since the APR-2 right swath side becomes the left swath side.
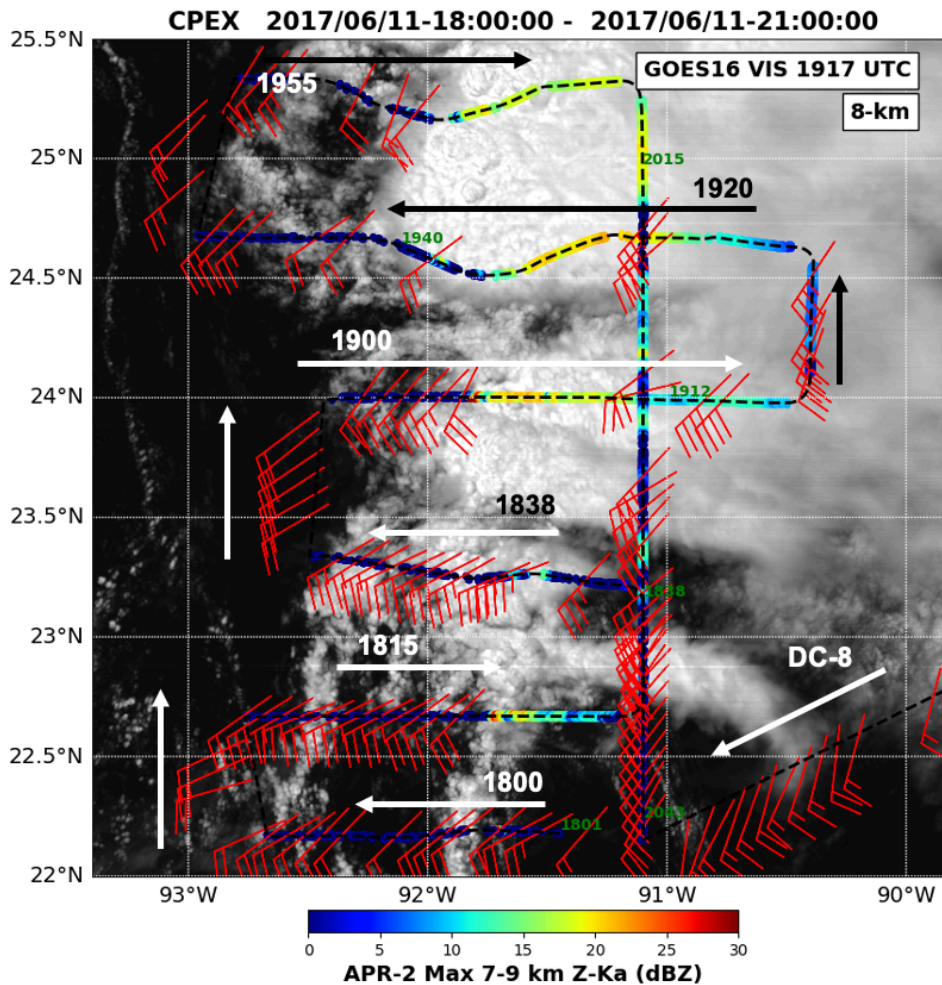
395

Figure 19. DC-8 flight lines during 1800-2130 UTC on 11 June. Same layout and format as Figure 4, but only for the 8-km level. The six E-W or W-E flight lines beginning near 1800, 1815, 1838, 1900, 1920 and 1955 UTC are shown.

400

The bottom panel of Figure 20 shows the APR-2 vertical (v_z) and across-track (v_y) winds estimated from (3) and (4), plotted in orange and black colors, respectively. DAWN (u, v) winds at the same 8-km level are shown in red and blue colors, respectively. Near 1830 UTC, the DAWN v component is near 5 m s^{-1}, and the APR-2 v component is near 5-10 m s^{-1}, but quickly (within a few minutes) changes to a smaller value as the DC-8 enters an area with stronger vertical motion and

405 assumptions on horizontal shear are likely voided. Near 1840 when the DC-8 is flying along a 270-degree bearing and detects clouds at the 8-km level, the APR-2 v component changes to -12 m s^{-1}. While it is the expected wind speed sign flip, it is more difficult to compare the wind speed magnitude. Also, the 270-degree bearing has some deviations near 1843 UTC to avoid convection at flight level.
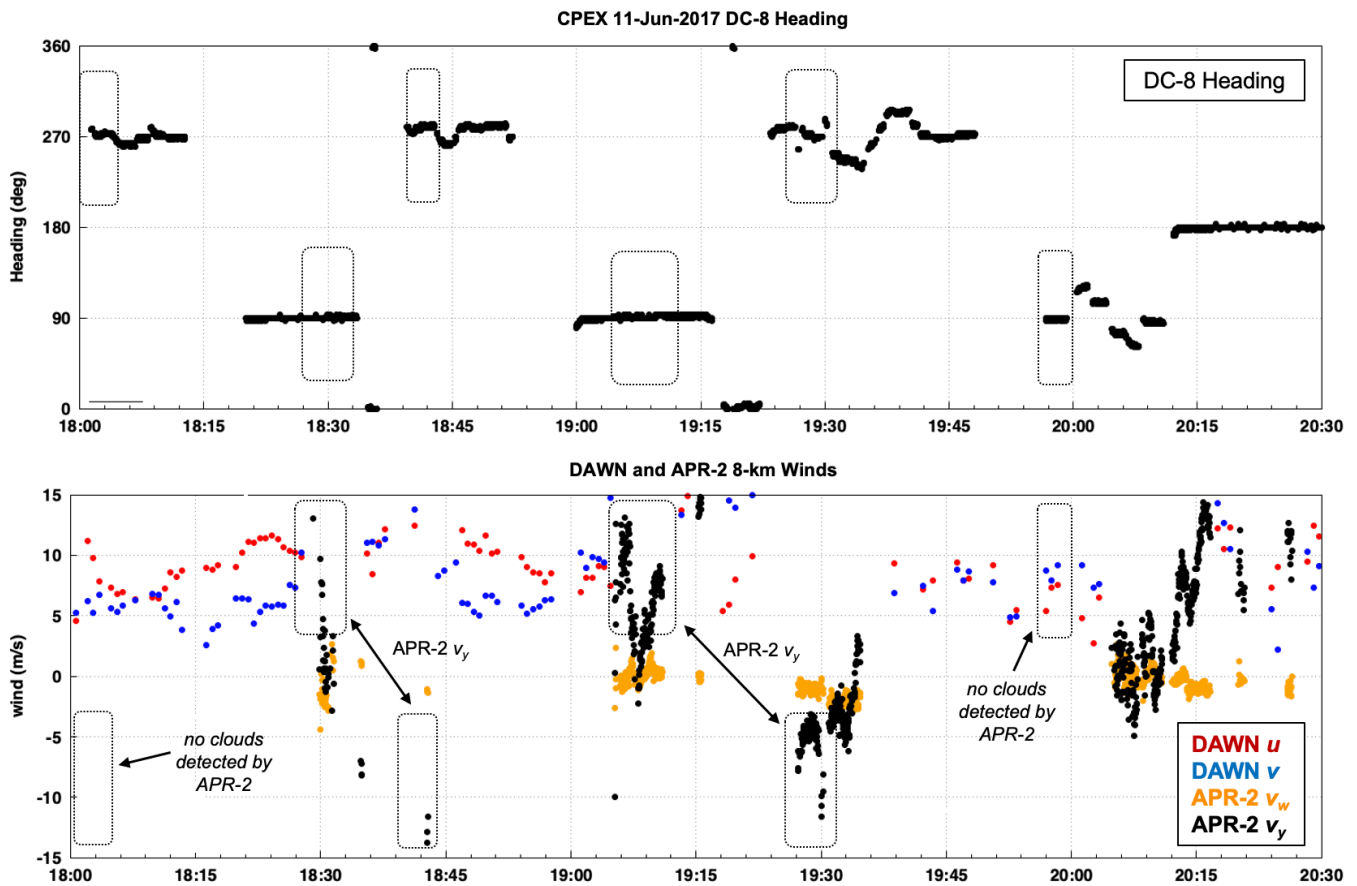
26

Figure 20. (Top) DC-8 heading between 1800-2130 UTC on 11 June 2017, highlighting the six time periods depicted in Figure 19. (Below) DAWN (*u, v*) wind vectors at the 8-km level (red and blue points, respectively). APR-2 (v_w, v_y) winds (orange and black, respectively) estimated from (3) and (4).

A second coincidence occurs between the APR-2 data near 1910 and 1925 UTC, where the APR-2 v_y component flips sign between similar wind speed values. However, the area at 1925 UTC is so cloud-filled that there are no nearby DAWN wind profile data to compare to. It also represents an area with stronger vertical winds, where the assumption of no significant horizontal shear across the APR-2 scan swath is likely not valid. While this is not a rigorous comparison of DAWN and Doppler precipitation radar horizontal winds, the principle could be applied to any these data from any close time pair of DC-8 flight bearing segments that are separated by 180-degrees. In this example, the flight bearings were fortuitously along easterly or westerly directions. For any arbitrary flight bearing, the cross-track winds estimated by (4) are more generally a combination of (*u, v*), and the DAWN (*u, v*) winds could be transformed to these same directions for comparison. This complement of Doppler radar and DWL observations could provide a means to link horizontal wind data outside of clouds and inside clouds (away from strong vertical motion, from APR-2), an important transition region. Space-based Doppler

27

radar measurement methods to estimate the horizontal LOS (HLOS) wind in-cloud have been proposed (*Illingworth et. al.*, 2018), as one means to complement the HLOS winds from Aeolus. However, further investigation from CPEX and other APR-2 airborne data are needed to assess the quality of the radar wind components before they can be used for science or model data assimilation purposes.

430 **5   Conclusions.**

This manuscript has presented joint observations from the DAWN Doppler wind lidar and the APR-2 (Ku/Ka-band) Doppler precipitation radar, collected during the CPEX campaign in 2017. Data from NASA DC-8 flight segments from two flight dates were examined to assess the ability of DAWN to sense air motion nearby to developing convection.   The flight patterns on June 10-11 were selected for this purpose. For the June 10 flight date, the DC-8 arrived on-station to the area of
435   interest, with sufficient time to capture the evolution of isolated, small-scale (< 10-km horizontal extent, many not yet glaciated) clouds from numerous DC-8 repeat passes for about a 3-hour period.   The environment surrounding the clouds on this date exhibited directional shear between the 2- and 8-km levels in the quadrant SW of the developing convection. A number of growing convective clouds with APR-2 echo tops below 5-km were sampled by the APR-2, away from the more developed convection. The capability of DAWN to collect LOS profiles near convection was highlighted for several passes
440   where profile retrievals were possible up to the edges of many APR-2 detected cloud systems.   On June 11, the DC-8 sampling pattern consisted of successive repeat passes on E-W and W-E flight bearings, where the cross-track winds from APR-2 were examined for consistency with nearby DAWN winds, in the proximity of cloud edges.

As stated in the introduction, this manuscript provides the observational context for a separate mesoscale model data
445   assimilation study, which is aimed at quantifying the impact of the DAWN measurements on the analyzed atmospheric state variables and on the forecasted precipitation when the DAWN wind profile observations were assimilated into the model (*Zhang et. al.*, 2019). While only limited examples are shown, these particular findings highlight the importance of when and where the wind observations are taken, and provide guidance for assessing observational strategies and requirements needed for future airborne field campaigns with similar instrumentation.

450 **Data Availability**

The DAWN LOS and profile data (ASCII text format) and APR-2 data (HDF5 format) are available from the authors upon request.

Team list

Author Contribution

455   ST, SLD and OS carried out the APR-2 data pre-processing to produce Level-1 reflectivity products. FJT carried out the data alignment between DAWN and APR-2.   All JPL authors contributed to operations of the APR-2 during CPEX. SG and GDE collected and performed all DAWN data processing.

Competing Interests

The authors declare that they have no conflict of interest.

References

Baker, W.E., Atlas, R., Cardinali, C., Clement, A., Emmitt, G.D., Gentry, B.M., Hardesty, R.M., Källén, E., Kavaya, M.J., Langland, R., Ma, Z., Masutani, M., McCarty, W., Pierce, R.B., Pu, Z., Riishojgaard, L.P., Ryan, J., Tucker, S., Weissmann, M., and Yoe, J.G.: Lidar-Measured Wind Profiles: The Missing Link in the Global Observing System. *Bull. Amer. Meteor.*
470   *Soc*. **95**, 543–564, https://doi.org/10.1175/BAMS-D-12-00164.1, 2014.

Black, M. L., Burpee, R. W., & Marks, F. D.: Vertical Motion Characteristics of Tropical Cyclones Determined with Airborne Doppler Radial Velocities. *Journal of the Atmospheric Sciences*, *53*(13), 1887–1909. https://doi.org/10.1175/1520-0469(1996)053<1887:VMCOTC>2.0.CO;2, 1996.
475

Black, P., Harrison, L., Beaubien, M., Bluth, R., Woods, R., Penny, A., Smith, R.W., and Doyle, J.D.: High-Definition Sounding System (HDSS) for Atmospheric Profiling. *J. Atmos. Oceanic Technol.,* **34**, 777–796, https://doi.org/10.1175/JTECH-D-14-00210.1, 2017.

480   Bucci, L. R., O'Handley, C., Emmitt, G. D., Zhang, J. A., Ryan, K., & Atlas, R.: Validation of an Airborne Doppler Wind Lidar in Tropical Cyclones. *Sensors (Basel, Switzerland)*, *18*(12), 4288. doi:10.3390/s18124288, 2018.

Chen, S.S., Kerns, B.W., Guy, N., Jorgensen, D.P., Delanoë, J., Viltard, N., Zappa, C.J., Judt, F., Lee, C.-Y., and Savarin, A.: Aircraft Observations of Dry Air, the ITCZ, Convective Cloud Systems, and Cold Pools in MJO during DYNAMO. Bull.
485   Amer. Meteor. Soc. **97**, 405–423, doi.org/10.1175/BAMS-D-13-00196.1, 2015.

Durden, S.L., Tanelli, S., and Im, E., 2012. Recent observations of clouds and precipitation by the airborne precipitation radar 2nd generation in support of the GPM and ACE missions. Proc. SPIE 8523, Remote Sensing of the Atmosphere, Clouds, and Precipitation IV, International Society for Optics and Photonics, 85230M, https://doi.org/10.1117/12.977574,
490   2012.

Durden, S.L., Li, L., Im, E., and Yueh, S.H.: A Surface Reference Technique for Airborne Doppler Radar Measurements in Hurricanes. J. Atmos. Oceanic Technol. **20**, 269–275, doi.org/10.1175/1520-0426(2003)020<0269:ASRTFA>2.0.CO;2, 2003.

495

Flamant, P., Cuesta, J., Denneulin, M.-L., Dabas, A., and Huber, D.: ADM-Aeolus retrieval algorithms for aerosol and cloud products. *Tellus A: Dynamic Meteorology and Oceanography* **60**, 273–286, 2008.

Guimond, S.R., Tian, L., Heymsfield, G.M., and Frasier, S.J.: Wind Retrieval Algorithms for the IWRAP and HIWRAP
500   Airborne Doppler Radars with Applications to Hurricanes. J. Atmos. Oceanic Technol. 31, 1189–1215, doi.org/10.1175/JTECH-D-13-00140.1, 2014.

Heymsfield, G.M., Bidwell, S.W., Caylor, I.J., Ameen, S., Nicholson, S., Boncyk, W., Miller, L., Vandemark, D., Racette, P.E., and Dod, L.R.: The EDOP Radar System on the High-Altitude NASA ER-2 Aircraft. J. Atmos. Oceanic Technol. 13,
505   795–809, doi.org/ 10.1175/1520-0426(1996)013<0795:TERSOT>2.0.CO;2, 1996.

Horányi, A., Cardinali, C., Rennie, M. and Isaksen, L.: The assimilation of horizontal line-of-sight wind information into the ECMWF data assimilation and forecasting system. Part I: The assessment of wind impact. Q.J.R. Meteorol. Soc., 141: 1223-1232. doi:10.1002/qj.2430, 2015.

510

Hristova-Veleva, S., Knosp, B., Li, P.P., Vu, Q., Turk, F.J., Lambrigtsen, B., Su, H., Chen, S., and Zipser, E.J.: CPEX Data Portal: Status and Updates.   *2nd CPEX Science Team Meeting*, 18-19 July, Univ. of Washington,

https://cpex.jpl.nasa.gov/scienceteammeeting/2019/SvetlaHristova-Veleva_Presentation1_CPEX_portals_2019_07_16_SHV_v02_final.pdf, 2019.

515

Illingworth, A.J., Battaglia, A., Bradford, J., Forsythe, M., Joe, P., Kollias, P., Lean, K., Lori, M., Mahfouf, J.-F., Melo, S., Midthassel, R., Munro, Y., Nicol, J., Potthast, R., Rennie, M., Stein, T.H.M., Tanelli, S., Tridon, F., Walden, C.J., and Wolde, M..: WIVERN: A New Satellite Concept to Provide Global In-Cloud Winds, Precipitation, and Cloud Properties. Bull. Amer. Meteor. Soc. 99, 1669–1687, doi.org/10.1175/BAMS-D-16-0047.1, 2018.

520

Jiang, H., Liu, C. and Zipser, E.J.: A TRMM-based Tropical Cyclone Cloud and Precipitation Feature Database. J. Appl. Meteor. Climatol., 50,1255-1274, doi.org/10.1175/2011JAMC2662.1, 2011.

Kavaya, M.J., Beyon, J.Y., Koch, G.J., Petros, M., Petzar, P.J., Singh, U.N., Trieu, B.C., and Yu, J.: The Doppler aerosol
525 wind (DAWN) airborne, wind-profiling coherent-detection Lidar system: overview and preliminary flight results. Journal of Atmospheric and Oceanic Technology 31, 826–842, doi.org/10.1175/JTECH-D-12-00274.1, 2014.

Lux, O., Lemmerz, C., Weiler, F., Marksteiner, U., Witschas, B., Rahm, S., Schäfler, A., and Reitebuch, O.: Airborne wind lidar observations over the North Atlantic in 2016 for the pre-launch validation of the satellite mission Aeolus. *Atmospheric*
530 *Measurement Techniques* *11*, 3297–3322, doi.org/10.5194/amt-11-3297-2018, 2018.

Okamoto, K., Ishibashi, T., Ishii, S., Baron, P., Gamo, K., Tanaka, T.Y., Yamashita, K., and Kubota, T.: Feasibility Study for Future Space-Borne Coherent Doppler Wind Lidar, Part 3: Impact Assessment Using Sensitivity Observing System Simulation Experiments. *J. Meteorol. Soc. of Japan. Ser. II* *96*, 179–199, doi.org/10.2151/jmsj.2018-024, 2018.

535

Pu, Z., Zhang, L., and Emmitt, G.D.: Impact of airborne Doppler Wind Lidar data on numerical simulation of a tropical cyclone , *Geophy. Res. Lett.*, **37**, L05801, doi:10.1029/2009GL041765, 2010.

Raymond, D., Fuchs, Ž., Gjorgjievska, S., Sessions, S.: Balanced dynamics and convection in the tropical troposphere.
540 *Journal of Advances in Modeling Earth Systems* **7**, 1093–1116, https://doi.org/10.1002/2015MS000467, 2015.

Rowe, A.K., and Houze, R.A.: Microphysical characteristics of MJO convection over the Indian Ocean during DYNAMO. Journal of Geophysical Research: Atmospheres 119, 2543–2554, doi.org/10.1002/2013JD020799, 2014.

545 Rowe, A.K., Rutledge, S.A., and Lang, T.J.: Investigation of Microphysical Processes Occurring in Organized Convection during NAME. Mon. Wea. Rev. **140**, 2168–2187, doi.org/10.1175/MWR-D-11-00124.1, 2012.

Sadowy, G. A., Berkun, A.C., Chun, W., Im, E. and Durden, S.L., Development of an advanced airborne precipitation radar. *Microwave J.,* 46 (1), 84-98, 2003.

550

Šavli, M., Žagar, N., and Anderson, J.L.: Assimilation of horizontal line-of-sight winds with a mesoscale EnKF data assimilation system. *Q. J. Royal Meteorol. Soc, 144*, 2133–2155, doi.org/10.1002/qj.3323, 2018.

Schiro, K.A., and Neelin, J.D.: Deep Convective Organization, Moisture Vertical Structure, and Convective Transition
555   Using Deep-Inflow Mixing. *J. Atmos. Sci. 76*, 965–987, *doi.org/10.1175/JAS-D-18-0122.1*, 2019.

Stoffelen, A., Pailleux, J., Källén, E., Vaughan, J.M., Isaksen, L., Flamant, P., Wergen, W., Andersson, E., Schyberg, H., Culoma, A., Meynart, R., Endemann, M., and Ingmann, P.: The atmospheric dynamics mission for global wind field measurement. Bull. Amer. Meteor. Soc. **86**, 73–88, doi.org/10.1175/BAMS-86-1-73, 2005.

560

Tanelli, S., Durden, S.L., and Im, E.: Simultaneous measurements of Ku- and Ka-band sea surface cross-sections by an airborne radar. *IEEE Geosci. Remote Sens. Lett*., **3**, 359–363, 10.1109/LGRS.2006.872929, 2006.

Velden, C., Daniels, J., Stettner, D., Santek, D., Key, J., Dunion, J., Holmlund, K., Dengel, G., Bresky, W., and Menzel, P:
565   Recent innovations in deriving tropospheric winds from meteorological satellites. Bull. Amer. Meteorol. Soc., 86, 205–224, doi.org/10.1175/BAMS-86-2-205, 2005.

Zhang, S., Hristova-Veleva, S., and Turk, F. J.:   Assimilating the DAWN winds: Impact on the precipitation and flow structure of the June 10 squall line.   *2nd CPEX Science Team Meeting*, 18-19 July, Univ. of Washington,.
570   https://cpex.jpl.nasa.gov/scienceteammeeting/2019/SaraZhang_SvetlaHristoveVeleva_JoeTurk_20190717_CPEX_Assimilat ingDAWN_June10_v05_final.pdf, 2019.

Zhang, J.A., Atlas, R., Emmitt, G.D., Bucci, L., Ryan, K.: Airborne Doppler Wind Lidar Observations of the Tropical Cyclone Boundary Layer. *Remote Sens*, *10*, 825, https://doi.org/10.3390/rs10060825, 2018.

575

Zipser, E.J., and M. Rajgopal.:L The June 10 case: Observations, satellite, DAWN, and dropsondes. *1st CPEX Science Team Meeting*,   7-8   June,   Univ.   of   Utah,   https://cpex.jpl.nasa.gov/scienceteammeeting/2018/Zipseretal.-%20forScienceTeamMeeting%20-V2.ppt, 2018.

580   Zipser, E.J., Twohy, C.H., Tsay, S.-C., Thornhill, K.L., Tanelli, S., Ross, R., Krishnamurti, T.N., Ji, Q., Jenkins, G., Ismail, S., Hsu, N. C., Hood, R., Heymsfield, G.M., Heymsfield, A., Halverson, J., Goodman, H.M., Ferrare, R., Dunion, J.P., Douglas, M., Cifelli, R., Chen, G., Browell, E.V., and Anderson, B.: The Saharan Air Layer and the Fate of African Easterly Waves—NASA's AMMA Field Study of Tropical Cyclogenesis. *Bull. Amer. Meteor. Soc.* **90**, 1137–1156, doi.org/10.1175/2009BAMS2728.1, 2009.

585

Zuidema, P., Torri, G., Muller, C., and Chandra, A.: A Survey of Precipitation-Induced Atmospheric Cold Pools over Oceans and Their Interactions with the Larger-Scale Environment. *Surv. Geophys* **38**, 1283–1305, https://doi.org/10.1007/s10712-017-9447-x 2017.

590